
Detached-Eddy Simulation of the Ground Transportation System

Stephen Maddox¹, Kyle D. Squires², Ken E. Wurtzler³ and James R. Forsythe³

¹ United States Air Force Academy, Colorado Springs, CO 80840,
C03Stephen.Maddox@usafa.edu,

² MAE Department, Arizona State University, Tempe, AZ 85287,
squires@asu.edu

³ Cobalt Solutions, Springfield, OH 45504, wurtzler@cobaltcfd.com,
forsythe@cobaltcfd.com

Predictions of the flow around the Ground Transportation System (GTS) have been obtained using Detached-Eddy Simulation (DES) and the Reynolds-averaged Navier-Stokes (RANS) equations. The computations were performed at a Reynolds number based on body width and the inlet freestream velocity of 2×10^6 . Calculations at 0° and 10° yaw were performed using unstructured grids comprised of approximately 6×10^6 elements (prisms and tetrahedra) and using the commercial flow solver *Cobalt*. No attempt is made to model laminar-to-turbulent transition, the predictions are of the fully turbulent solution obtained via prescription of a small level of eddy viscosity at the inlet to the computational domain. The RANS predictions are of the steady-state solution using the Spalart-Allmaras model. For 0° yaw the predicted drag coefficient C_d from the RANS of 0.370 is substantially larger than the measured value of 0.249. DES yields a more complex and three-dimensional structure in the separated regions. One of the improvements over RANS is a more accurate prediction of the back pressures, resulting in the DES prediction of $C_d = 0.279$ being more accurate than the RANS result. At 10° yaw, DES predictions of the body-axis drag are closer to measurements than obtained using RANS, though substantially larger than the measured value. One source of the discrepancy is a more significant separated region near the front leeward corner than observed in experiments, resulting in more significant differences in the pressure distribution along the lee side.

1 Introduction and Overview

Computational Fluid Dynamics (CFD) is a useful tool for analysis and is increasingly relied upon in the design process for applications within the trans-

portation industry. Emphasis on fuel efficiency, for example, will require innovative approaches to vehicle design and testing. For heavy trucks at typical highway speeds the power to overcome aerodynamic drag accounts for more than half of the total fuel consumption[1]. CFD offers a powerful approach that should be able to efficiently screen configurations, prior to more costly and time-consuming wind-tunnel and field tests.

Prediction of the flow fields around complex configurations and for regimes of technological interest continues to strongly challenge CFD. Many of the regimes in vehicle aerodynamics occur at high Reynolds numbers and for which much of the flow around the configuration of interest is turbulent. Turbulence treatments at application Reynolds numbers are one of the primary obstacles in the advancement of CFD as a more routinely applied tool in engineering analysis and design.

Especially problematic in predicting the flow around vehicles at high Reynolds numbers are regions of massive separation. For many engineering systems, high-Reynolds number predictions are obtained from solutions of the Reynolds-averaged Navier-Stokes (RANS) equations. While the most popular RANS models appear to yield predictions of useful accuracy in attached flows as well as some with shallow separations, RANS predictions of massively separated flows have typically been uneven. In vehicle wakes, for example, it is not anticipated that RANS will provide accurate predictions of back pressures and, therefore, of the drag. In addition, in many studies that focus on techniques for reducing drag, alterations to the vehicle geometry result in strong modifications of the flow in the wake, precisely the region for which RANS modeling is the least reliable. Other approaches that offer higher-fidelity (and presumably greater accuracy) than RANS and are numerically feasible today are desired for applications.

The issues outlined above provided part of the motivation for detailed experimental studies of the Ground Transportation System (GTS) for which a series of experimental measurements were reported by Storms *et al.* [3]. The GTS is a simplified tractor-trailer configuration, the geometry is rounded without a tractor-trailer gap and without wheels. Measurements were acquired in the NASA-Ames 7×10 ft wind tunnel for a range of Reynolds numbers, yaw angles ranging from -14 to 14 degrees in 2.5 degree increments, and a Reynolds number range from 3×10^5 to 2×10^6 . Storms *et al.* [3] acquired pressure measurements at several locations on the GTS, in addition to measurements of the drag, spectra of the pressure fluctuations, and Particle-Image-Velocimetry measurements in the wake. One of the key contributions of the study was investigation of the influence of boattail plates mounted on the base of the GTS and used to investigate drag reduction.

The objective of the current effort is prediction of the flow field for a subset of the conditions considered by Storms *et al.* [3]. The approach adopted in the present investigation is prediction of the flow around the GTS using Detached-Eddy Simulation (DES). DES is a hybrid method which has RANS behavior near the wall and becomes a Large Eddy Simulation in the regions

away from solid surfaces provided the grid density is sufficient [2]. The formulation of the model used in this work is based on a modification to the Spalart-Allmaras one-equation model [4], referred to as S-A throughout and described in greater detail in the next section. DES is a non-zonal technique that is computationally feasible for high Reynolds number prediction, but also resolves time-dependent, three-dimensional turbulent motions as in LES. Previous applications of the method have been favorable, yielding adequate predictions across a range of flows and also showing the computational cost has a weak dependence on Reynolds number, similar to RANS methods yet at the same time providing more realistic descriptions of unsteady effects (see also [5]). This paper presents simulations for two yaw angles, 0° and 10° , using DES. The predictions are assessed against experimental measurements[3] as well against solutions of the steady-state flow obtained using the Spalart-Allmaras[4] one-equation model.

2 Approach

2.1 Detached Eddy Simulation

The DES formulation is based on a modification to the Spalart-Allmaras RANS model [4] such that the model reduces to its RANS formulation near solid surfaces and to a subgrid model away from the wall [2]. The Spalart-Allmaras RANS model solves an equation for the variable $\tilde{\nu}$ which is dependent on the turbulent viscosity. The model is derived based on empiricism and arguments of Galilean invariance, dimensional analysis and dependence on molecular viscosity. The model includes a wall destruction term that reduces the turbulent viscosity in the laminar sub-layer and trip terms to provide smooth transition to turbulence. The transport equation for the working variable $\tilde{\nu}$ used to form the eddy viscosity takes the form,

$$\begin{aligned} \frac{D\tilde{\nu}}{Dt} = c_{b1}\tilde{S}\tilde{\nu} - \left[c_{w1}f_w - \frac{c_{b1}}{\kappa^2}f_{t2} \right] \left[\frac{\tilde{\nu}}{d} \right]^2 \\ + \frac{1}{\sigma} \left[\nabla \cdot ((\nu + \tilde{\nu})\nabla\tilde{\nu}) + c_{b2}(\nabla\tilde{\nu})^2 \right], \end{aligned} \quad (1)$$

where $\tilde{\nu}$ is the working variable. The eddy viscosity ν_t is obtained from,

$$\nu_t = \tilde{\nu} f_{v1} \quad f_{v1} = \frac{\chi^3}{\chi^3 + c_{v1}^3} \quad \chi \equiv \frac{\tilde{\nu}}{\nu} \quad (2)$$

where ν is the molecular viscosity. The production term is expressed as,

$$\tilde{S} \equiv S + \frac{\tilde{\nu}}{\kappa^2 d^2} f_{v2}, \quad f_{v2} = \left(1 + \frac{\chi}{c_{v2}} \right)^{-3}, \quad (3)$$

where S is the magnitude of the vorticity. The function f_w is given by,

$$f_w = g \left[\frac{1 + c_{w3}^6}{g^6 + c_{w3}^6} \right]^{1/6}, \quad g = r + c_{w2} (r^6 - r), \quad r \equiv \frac{\tilde{\nu}}{\tilde{S} \kappa^2 d^2}. \quad (4)$$

The wall boundary condition is $\tilde{\nu} = 0$. The constants are $c_{b1} = 0.1355$, $\sigma = 2/3$, $c_{b2} = 0.622$, $\kappa = 0.41$, $c_{w1} = c_{b1}/\kappa^2 + (1 + c_{b2})/\sigma$, $c_{w2} = 0.3$, $c_{w3} = 2$, $c_{v1} = 7.1$, $c_{v2} = 5$, $c_{t1} = 1$, $c_{t2} = 2$, $c_{t3} = 1.1$, and $c_{t4} = 2$.

In DES, the aim is to apply the S-A model in attached regions, taking advantage of its adequate performance in the thin shear layers comprising its calibration range. In detached regions, the closure is modified such that the model yields a subgrid viscosity and the computation, provided the grid density is sufficient, becomes a Large Eddy Simulation, exploiting the capability of LES for resolution of geometry-dependent and three-dimensional eddies. The DES formulation is obtained by replacing in the S-A model the distance to the nearest wall, d , by \tilde{d} , where \tilde{d} is defined as,

$$\tilde{d} \equiv \min(d, C_{DES} \Delta). \quad (5)$$

In (5), Δ is the largest distance between the cell center under consideration and the cell center of the neighbors (i.e., those cells sharing a face with the cell in question). In “natural” applications of DES, the wall-parallel grid spacings (e.g., streamwise and spanwise) are on the order of the boundary layer thickness and the S-A RANS model is retained throughout the boundary layer, i.e., $\tilde{d} = d$. Consequently, prediction of boundary layer separation is determined in the “RANS mode” of DES. Away from solid boundaries, the closure is a one-equation model for the sub-grid scale eddy viscosity. When the production and destruction terms of the model are balanced, the length scale $\tilde{d} = C_{DES} \Delta$ in the LES region yields a Smagorinsky-like eddy viscosity $\tilde{\nu} \propto S \Delta^2$. The additional model constant $C_{DES} = 0.65$ was set in homogeneous turbulence[6].

2.2 Flow solver and grid

The compressible Navier-Stokes equations are solved on unstructured grids using *Cobalt* [7]. The numerical method is a cell-centered finite volume approach applicable to arbitrary cell topologies (e.g, hexahedrons, prisms, tetrahedrons). The spatial operator uses the exact Riemann Solver of Gottlieb and Groth[8], least squares gradient calculations using QR factorization to provide second order accuracy in space, and TVD flux limiters to limit extremes at cell faces. A point implicit method using analytic first-order inviscid and viscous Jacobians is used for advancement of the discretized system. For time-accurate computations, a Newton sub-iteration scheme is employed, the method is second order accurate in time. The domain decomposition library ParMETIS [9] is used for parallel implementation and provides optimal load balancing with a minimal surface interface between zones. Communication between processors is achieved using Message Passing Interface.

In the following, lengths are non-dimensionalized by the GTS width w , x identifies the longitudinal axis of the GTS, y is the coordinate normal to the

lower tunnel wall, and z identifies the spanwise dimension. In terms of the GTS width w , the total length is $7.647w$ and height is $1.392w$. The computational domain included the sidewalls and upper tunnel walls (including their one degree divergence). The no-slip condition was applied on the tunnel walls and the boundary layers were resolved. The upstream section of the computational domain was extended approximately $15w$ in front of the GTS in order that the boundary layer on the lower wall develop the same thickness as measured at the inlet to the test section in Storms *et al.* [3]. The exit boundary of the computational domain was located approximately $13.5w$ from the rear surface of the GTS.

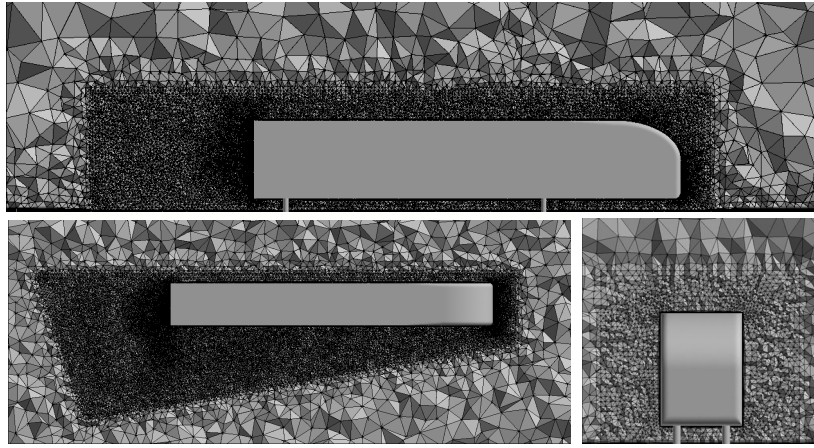


Fig. 1. Side, top, and front views of the GTS. Top view shown in lower-left frame shows the grid in a plane for the computations of the flow at 10° yaw with a clustering of cells into the leeward region. Front view shows grid clustering around both sides of the GTS for the computations at 0° yaw.

The unstructured grids were generated using Gridgen[10], with prisms in the boundary layer and tetrahedra elsewhere. The wall-normal distribution of cells was clustered near solid surfaces such that average distance to the first cell center from the wall was less than one viscous unit. The grids were comprised of approximately 6×10^6 cells. Shown in Figure 1 are front, side, and top views of the GTS along with crinkle cuts of the grid. Each of the views shows a clustering of grid cells in the vicinity of the GTS, with the side view in Figure 1 showing a biasing of points into the wake region behind the GTS. This clustering is achieved by using Gridgen's multiblock capability. The top view in the figure shows a cut of the grid used for the computations of the flow at 10° yaw. A wedge-shaped distribution of finer resolution is shaded into the leeward region in order to provide improved resolution of the separated structures along the leeward side. The front view in the figure is from the grid

used in the computations at 0° yaw, a symmetric grid clustering is evident in the frame.

3 Results

Summarized in this section are DES and RANS predictions of the flow around the GTS for yaw angles of 0° and 10° . The DES predictions are of the unsteady flow, the dimensionless timestep (non-dimensionalized using the GTS width w and upstream speed U_{in}) was 0.02. RANS predictions presented in this manuscript are of the steady-state solution, obtained on the same grids as the DES results, the calculations having been driven to convergence in computations performed using very large timesteps (corresponding to a global CFL number of 10^6).

3.1 Flow structure

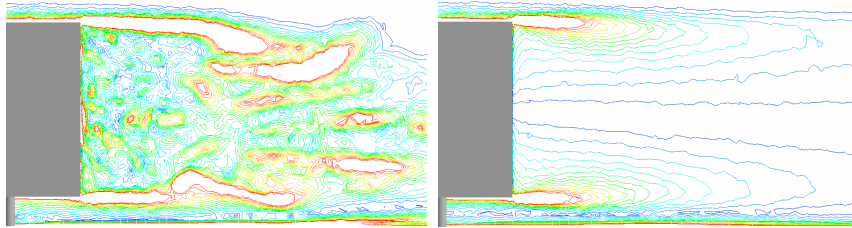


Fig. 2. Contours of the instantaneous vorticity in the GTS wake from the DES (left frame) and of the steady-state vorticity from the RANS (right frame).

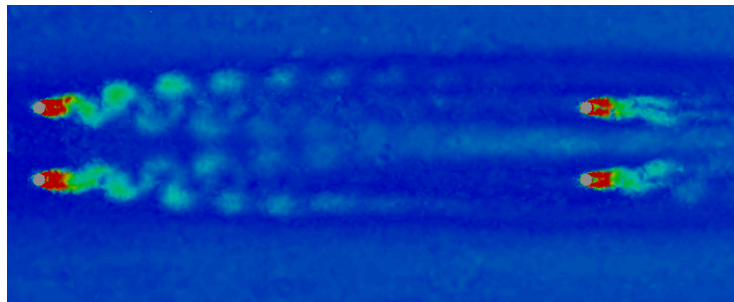


Fig. 3. Contours of the instantaneous vorticity in a plane midway between the lower tunnel wall and lower surface of the GTS. DES prediction of the flow at 0° yaw.

Shown in Figure 2 are contours of the instantaneous vorticity in the wake of the GTS predicted in the DES (left frame of Figure 2) and steady-state distribution from the RANS (right frame of Figure 2). The centerplane is shown from computations of the flow at 0° yaw. As shown in the figure, the wake resolved in the steady-state RANS is formed between two shear layers from the top and bottom of the GTS with a smooth diffusion of the vorticity from the shear layers as evident in the figure. In the DES, a range of eddies is resolved in the wake down to roughly the grid scale as shown in the figure. Figure 3 shows vorticity contours of the instantaneous solution predicted in the DES at 0° yaw in a plane parallel and midway between the lower tunnel wall and lower surface of the GTS. The posts on which the GTS was mounted were included in the computations and as shown by the figure, the grid used for the time-dependent DES prediction was sufficiently fine to resolve vortex shedding in the wake of the posts.

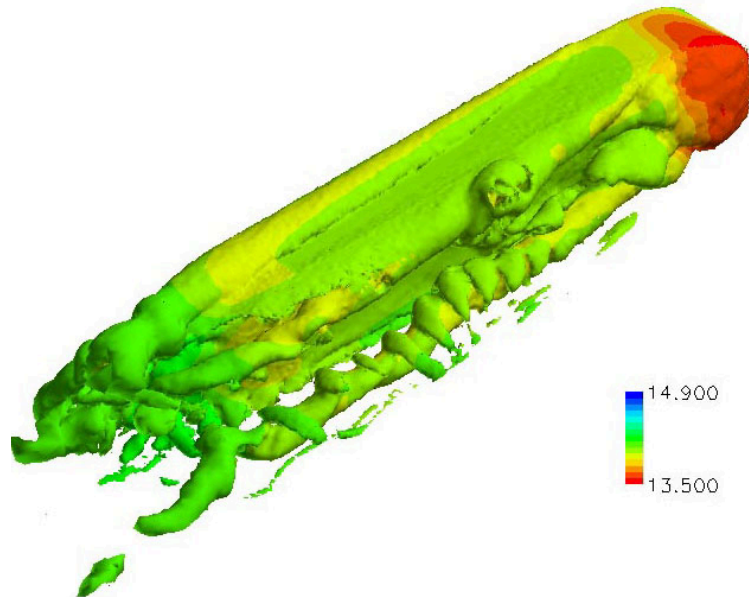


Fig. 4. Instantaneous vorticity isosurface colored by pressure from the DES, 10° yaw.

A vorticity isosurface (colored by pressure) is shown in Figure 4 from the DES prediction of the flow at 10° yaw. The figure shows the development of the roof vortex that develops from the front, windward region of the GTS. As shown in Figure 14 below, the skin friction along the upper surface of the GTS is strongly influenced by the roof vortex. Along the leeward region, Figure 4 shows two dominant structures that emanate from the roof and lower

surface of the GTS. The structure nearest the lower wall interacts strongly with the ground. Secondary structures, the horseshoe-shaped vortices that are apparent approximately halfway down the GTS length, that develops around the main structure are also resolved. Figure 4 also shows the strong three-dimensionality in the wake behind the rear surface of the GTS.

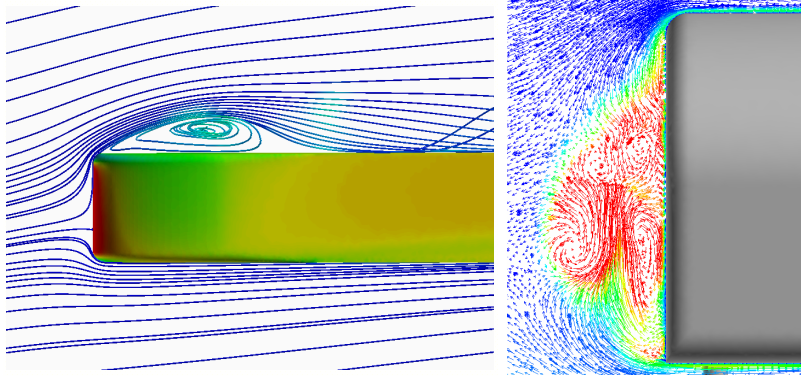


Fig. 5. Streamlines (left frame) and velocity vectors (right frame) from the DES prediction of the flow at 10° yaw. GTS surface colored by pressure in the left frame, velocity vectors colored by the eddy viscosity ratio in the right frame.

Also apparent in Figure 4 is a separated region near the front leeward side of the GTS. Two views through the separated region are shown in Figure 5. The top view is a plane at $y = 0.696w$ (midway from the lower surface to the roof of the GTS) and shows a separation bubble with reattachment at approximately $x/w \approx 0.2$, substantially further along the GTS than indicated by pressure measurements in Storms *et al.* [3]. The front view in the right frame of Figure 5 shows the counter-rotating structures that “close” the separation bubble.

3.2 Flow Statistics

Shown in Figure 6 are the time histories of DES predictions of the body-axis drag coefficient C_d and side force coefficient C_s . Only a portion of the force histories from a statistically-stationary portion of the simulation are shown (statistics were acquired for more than $80w/U_{in}$). The figure shows that for both yaw angles the variations in the body-axis drag are smaller than occurring in the side force. For 0° yaw the side-force coefficient shows a lower-frequency meandering that occurs at a Strouhal number around 0.2. For 10° degrees yaw, a less apparent low-frequency component in C_s is observed.

Summarized in Table 1 are the time-averaged body-axis and side force coefficients from the DES and RANS. Also tabulated are the experimental

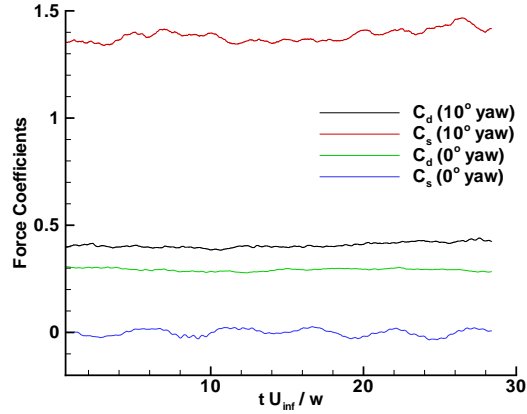


Fig. 6. Temporal evolution of the body-axis drag coefficient, C_d , and side-force coefficient, C_s , from the DES predictions of the flow at 0° and 10° yaw.

measurements from Storms *et al.* [3]. At 0° yaw, the RANS prediction of the drag coefficient is substantially larger than the measured value of 0.249 from Storms *et al.* [3]. The DES prediction is only 12% over the measured value, the realistic treatment of the separated region in the GTS wake responsible for the improved predictions of the drag force (see also Figure 7). For 10° yaw both the DES and RANS predictions of the body-axis drag coefficient are above the measured value, slightly better agreement between simulations and measurements is observed in the side-force coefficient.

Table 1. Mean body-axis force coefficients.

yaw	DES	RANS	measured
$C_d, \beta = 0^\circ$:	0.279	0.370	0.249
$C_d, \beta = 10^\circ$:	0.406	0.462	0.292
$C_s, \beta = 10^\circ$:	1.379	1.306	1.253

Pressure coefficients were calculated following a similar approach as in the experiments, using as a reference the wall pressure along the sidewall at the same location as in the experiments of Storms *et al.* [3]. Shown in Figure 7 and Figure 8 are the symmetry plane pressure coefficients for the GTS at 0° and 10° yaw, respectively. The pressure coefficients are plotted as a function of the vertical coordinate in order to provide an indication of the drag. In general, both figures show that the stagnation pressure on front of the GTS is captured with the acceleration around the front face also accurately recovered. The pressure distributions predicted by the DES and RANS on the front face

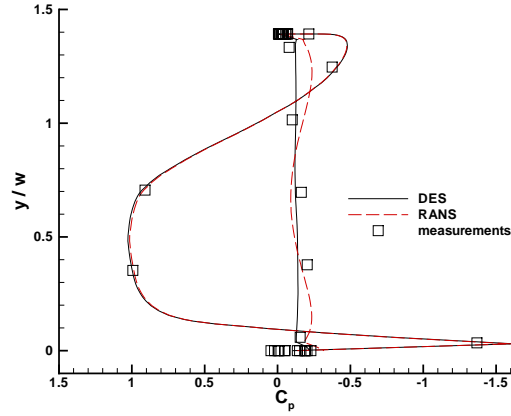


Fig. 7. Centerplane pressure coefficients, $\beta = 0^\circ$

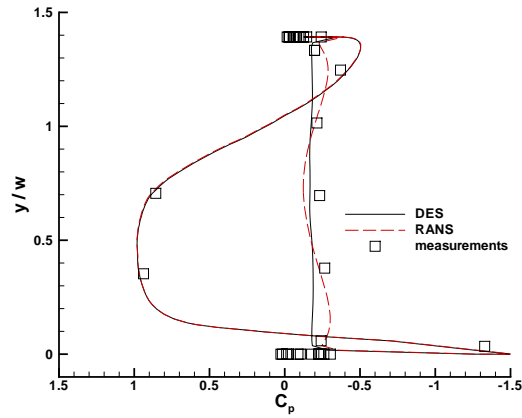


Fig. 8. Centerplane pressure coefficients, $\beta = 10^\circ$

are essentially identical, differences between the two techniques are apparent along the rear surface. The DES prediction of the pressure coefficient exhibits relatively little sensitivity to the vertical coordinate and is nearly uniform, characteristic of the uniform pressure over surfaces in the separated regions of massively separated flows. The RANS prediction, on the other hand exhibits more substantial variation with a relatively strong suction near the upper and lower surfaces. This in turn leads to an over-prediction of the drag.

Pressures along the top of the GTS for 0 and 10 degrees yaw are shown in Figure 9 and Figure 10, respectively. The pressures are plotted along the GTS centerline ($z/w = 0$) on the top of the model ($y/w = 1.392$). The effect of the model surface curvature above the cab results in a suction peak of

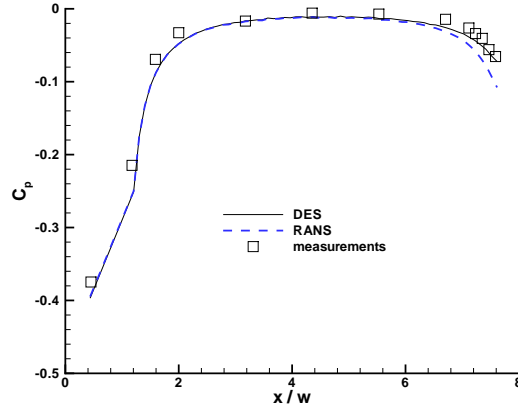


Fig. 9. Pressure coefficient along the GTS centerline, $\beta = 0^\circ$.

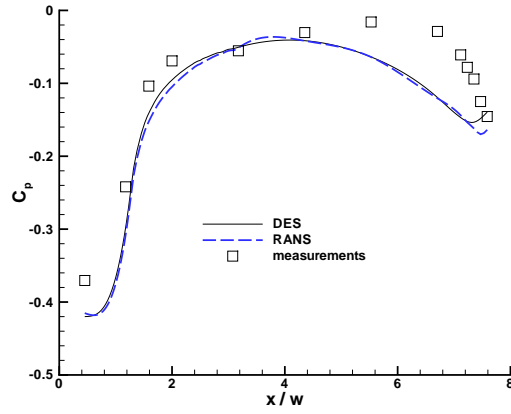


Fig. 10. Pressure coefficient along the GTS centerline, $\beta = 10^\circ$.

about $C_p \approx -0.4$ in the figure. The pressure is then relatively constant and subsequently decreases in response to the flow acceleration to the streamline curvature into the wake, the reduction in the pressure coefficient for the GTS at 10° yaw being more significant because of the higher speed flow over the top of the GTS, resulting from the relatively greater blockage of the tunnel caused for the geometry at sideslip. In general, both the DES and RANS predict reasonably accurately the acceleration of the flow over the front surface of the GTS. For 0° yaw the DES prediction of the slight decrease in C_p near the rear surface in Figure 9 is more accurate in the DES than the RANS. At 10° yaw, Figure 10 shows that both the DES and RANS predictions of the pressure

coefficient exhibit a more gradual reduction compared to the experimental measurements of Storms *et al.* [3].

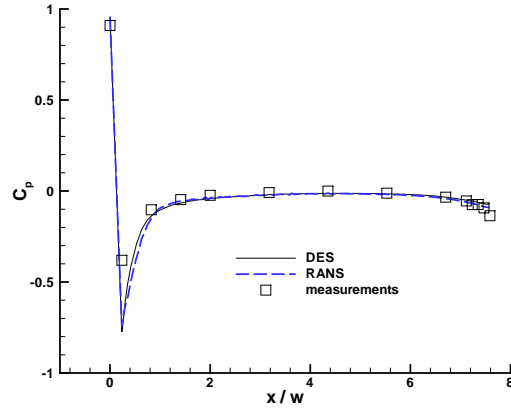


Fig. 11. Pressure distribution along the side of the GTS, $\beta = 0^\circ$.

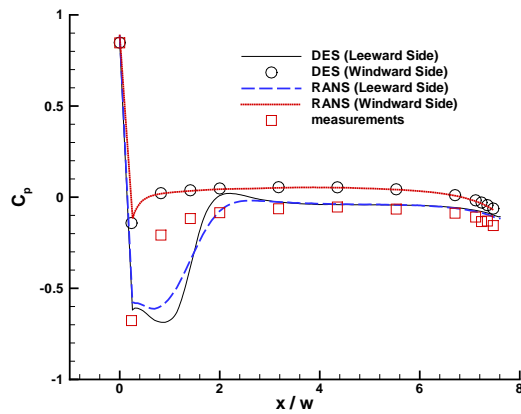


Fig. 12. Pressure distribution along the side of the GTS, $\beta = 10^\circ$.

Pressures along the side of the GTS are shown for both yaw angles in Figure 11 and Figure 12. The distributions were measured at $y/w = 0.696$ (midway between the lower GTS surface and roof) and in the experimental configuration on the left side of the configuration, corresponding to the windward side for the computations at positive 10° yaw. The pressure distribution for 0° yaw in Figure 11 shows that at $x/w = 0$ a pressure near stagnation is

recovered, as expected. The pressure decreases very significantly due to the acceleration around the front corner and is then relatively constant to the end of the trailer. The acceleration due to the converging streamlines into the wake is captured in both the DES and RANS and in good agreement with the measurements. Though not obvious from Figure 11, the DES prediction is in slightly better agreement with measurements near the end of the trailer.

For 10° yaw the pressure distributions along the side of the GTS are shown for both the leeward and windward side along with the measurements of C_p which were acquired along the leeward side of the GTS. Figure 12 shows that on the windward side of the GTS analogous features as observed in Figure 11 are observed, i.e., a sharp reduction in the pressure as the flow turns the front corner of the model with a roughly constant distribution to the end of the trailer and then slight reduction due to the flow acceleration into the wake. As evident in the figure, the RANS and DES descriptions of the pressure distribution along the windward side are very similar. The leeward side pressure distribution shows the largest differences between the RANS and DES near the front corner (“passenger side”). A stronger suction is predicted by both simulation techniques, an effect that arises due to the substantially larger region of flow separation predicted than measured (c.f., Figure 5). The discrepancy in the pressure distribution in this region in turn leading to larger discrepancies in the predicted forces at 10° yaw compared to the results at 0° yaw.

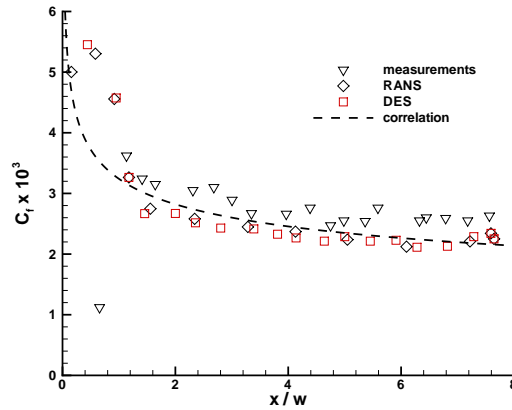


Fig. 13. Skin friction magnitude in the centerplane, $\beta = 0^\circ$.

A plot of the skin-friction magnitude along the centerline of the top of the GTS is shown in Figure 13 and Figure 14 for the GTS at 0 and 10 degrees yaw, respectively. Also included in each figure is the theoretical curve for skin friction on a turbulent flat plate. In the experiments reported by Storms *et*

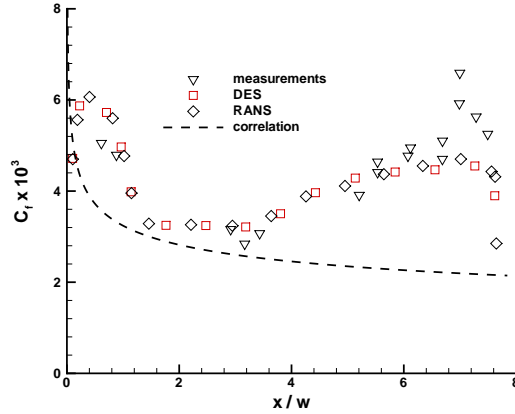


Fig. 14. Skin friction magnitude in the centerplane, $\beta = 10^\circ$.

al. [3] the boundary layers were not tripped, the measurements in Figure 13 show that the boundary layer is initially laminar before rapidly increasing to values characteristic of turbulent boundary layers following transition. In the simulations (both DES and RANS) the eddy viscosity at the inlet to the computational domain is non-zero (prescribed as three times the molecular value), an effect that ignites the turbulence model as the fluid enters the boundary layers. Consequently, C_f is larger than the experimental measurements near the front of the GTS. Figure 13 shows that the experimental measurements are slightly above the flat-plate correlation, the simulations slightly below.

The effect of non-zero yaw on the skin friction is apparent in the skin friction along the GTS centerline shown in Figure 14. For reference, the same curve for a flat-plate turbulent boundary layer as shown in Figure 13 is also shown in Figure 14. In the vicinity $x/w = 0$, the DES and RANS predictions are similar to the distributions for 0° yaw and also in good agreement with measurements. At approximately the mid-region of the GTS (slightly upstream of $x/w \approx 4$), the influence of the roof vortex is apparent via the increase in C_f as shown in the figure. DES and RANS predictions are again similar and also in good agreement with measurements. Near $x/w = 8$ the experimental measurements show a relatively sharp increase in C_f that is not reflected in the calculations.

4 Summary

The work reported in this manuscript represents the findings from an initial set of investigations that were aimed at gaining some insight into the application of DES to vehicle aerodynamics. The principal comparisons were to experimental measurements of Storms *et al.* [3] as well as assessment of DES

predictions against RANS results obtained for the steady-state flow. Overall, the results are encouraging in that for mean quantities DES is superior to RANS, e.g., predictions of the drag were in substantially better agreement with measured values at 0° yaw.

At 10° yaw the differences in measured and predicted forces were more substantial. The computations were of the fully-turbulent flow, i.e., without the use of the trip terms in the S-A model to dictate the location of laminar-to-turbulent transition. Some of the discrepancy in the force predictions at 10° yaw may be connected to the laminar or turbulent state of the boundary layers. Relevant in this regard is the front corner region in which the separation is more substantial in the simulations than indicated by measurements. The corner radius of the GTS challenges the RANS region and transition prediction – the complexity is also manifest in the hysteresis of the drag coefficient with Reynolds number observed in the experiments. Tests with less-rounded geometries would enable some resolution of these issues, more clear-cut from the standpoint of flow physics but possibly more challenging of computational aspects.

In addition to these aspects, there remain issues for which further investigations are also motivated. The role of the grid was not assessed, grid generation for the current effort was guided by experience developed by the investigators in previous DES applications to complex configurations. Coupled with an investigation of the grid would be related efforts to explore the timestep. Within the context of the present approach using the S-A model, prescribing the location of transition is possible and would enable interesting investigations of, for example, tripping the top surface boundary layers while employing the tripless approach of Travin *et al.* [11] for the sides of the GTS. As also summarized above, aspects related to geometrical features such as the influence of the corner radius of the model should be investigated. Finally, the influence of boattails plates to reduce drag reduction is well documented by Storms *et al.* [3] and any future efforts employing large-scale simulations should develop a simulation plan for investigation of such effects.

5 Acknowledgments

The authors are grateful for the helpful suggestions provided throughout the project by Dr. Philippe Spalart. Dr. Bruce Storms kindly provided the experimental measurements in electronic format. Discussions of the GTS grids with Dr. Chris Roy are also gratefully acknowledged.

References

1. McCallen R, Couch R, Hsu J, Leonard A, Brady M, Browand F, Hammache M, Salari K, Rutledge W, Ross J, Storms B, Heineck JT, Driver D, Bell J, Zilliac G

- (1999) Progress in Reducing Aerodynamic Drag for Higher Efficiency of Heavy Duty Trucks (Class 7-8), 1999-01-2238, Gov/Industry Meeting, Washington, DC.
2. Spalart PR, Jou WH, Strelets M, Allmaras SR (1997) Comments on the feasibility of LES for wings, and on a hybrid RANS/LES approach. 1st AFOSR Int. Conf. on DNS/LES, Aug. 4-8, 1997, Ruston, LA. In *Advances in DNS/LES*, C. Liu and Z. Liu Eds., Greyden Press, Columbus, OH, USA.
 3. Storms BL, Ross JC, Heineck, JT, Walker SM, Driver DM, Zilliac GG (2001) An experimental study of the Ground Transportation System (GTS) model in the NASA Ames 7- by 10-ft wind tunnel. *NASA/TM-2001-209621*.
 4. Spalart PR, Allmaras SR (1994) A One-Equation Turbulence Model for Aerodynamic Flows. *La Recherche Aerospatiale*, **1**, pp. 5-21.
 5. Strelets M (2001) Detached Eddy Simulation of Massively Separated Flows *AIAA 01-0879*.
 6. Shur ML, Spalart PR, Strelets MK, Travin AK (1999) Detached-Eddy Simulation of an Airfoil at High Angle of Attack. *Fourth International Symposium on Engineering Turbulence Modelling and Measurements*, Corsica, France.
 7. Strang WZ, Tomaro RF, Grismer MJ (1999) The Defining Methods of Cobalt₆₀: a Parallel, Implicit, Unstructured Euler/Navier-Stokes Flow Solver. *AIAA 99-0786*.
 8. Gottlieb JJ, Groth CPT (1988) Assessment of Riemann Solvers for Unsteady One-Dimensional Inviscid Flows of Perfect Gases *Journal of Computational Physics*, **78**, pp. 437-458.
 9. Karypis G, Schloegel K, Kumar V (1997) ParMETIS: Parallel Graph Partitioning and Sparse Matrix Ordering Library Version 1.0. University of Minnesota, Department of Computer Science, Minneapolis, MN 55455.
 10. Steinbrenner J Wyman N, Chawner J (2000) Development and Implementation of Gridgen's Hyperbolic PDE and Extrusion Methods. *AIAA 00-0679*.
 11. Travin A, Shur M, Strelets M, Spalart PR (2000) Detached-Eddy Simulations past a Circular Cylinder. *Flow, Turb. Comb.* **63**, pp. 293-313.